Optically Stable Biocompatible Flame-Made SiO$_2$-Coated Y$_2$O$_3$: Tb^{3+} Nanophosphors for Cell Imaging

Georgios A. Sotiriou,[†,§,*] Davide Franco,[‡,§] Dimos Poulikakos,[‡,*] and Aldo Ferrari[‡]

[†]Particle Technology Laboratory, Institute of Process Engineering and [‡]Laboratory of Thermodynamics in Emerging Technologies, Institute of Energy Technology Department of Mechanical and Process Engineering, ETH Zurich, Sonneggstrasse 3, 8092 Zurich, Switzerland. [§]Contributed equally to this work.

The range of potential applications of nanoscale materials in biomedical research has significantly expanded in the past few years.[1] In particular, light-emitting nanoparticles can be employed in bioimaging applications,[2] as they outperform the commonly used fluorescent organic dyes. In fact, a major drawback of organic dyes is optical instability, which leads to fast photobleaching and limits the analysis and interpretation of data. Semiconducting nanoparticles (quantum dots; QDs)[3] represent an established alternative to organic dyes.[4] The peak emission wavelength of QDs can be finely modulated depending on the particle size, and the resulting fluorescent signal does not degrade significantly upon excitation. However, QDs may exhibit blinking,[5] and their biocompatibility is not optimal, as they typically contain heavy metals such as Cd or Pb, which interfere with biological activities.[6,7]

Nanophosphors are light-emitting nanoparticles that contain a rare earth element dispersed in a crystal host matrix.[8] The resulting optical properties do not depend on the nanoparticle size, but on the chosen element. Nanophosphors do not degrade significantly upon excitation and are generally less toxic than QDs;[9] however their emission efficiency critically depends on the crystallinity of the host matrix. Indeed, due to their small size and the large surface-to-volume ratio, these nanoparticles frequently present crystal defects[10] that reduce their optical performance. An annealing process step is therefore generally required to eliminate any crystal defect, thus improving their crystallinity.[11] The annealing process, however, can induce the formation of sinter necks and aggregates that increase the nanophosphors size, limiting their use in bioimaging applications.[12,13]

Recently, processes involving high temperatures, such as flame aerosol synthesis,[14]

ABSTRACT
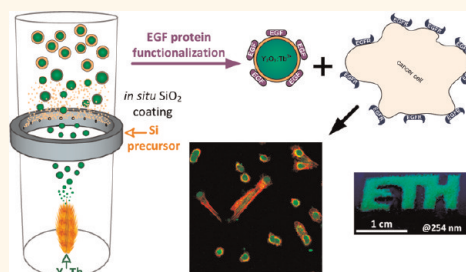
Nanophosphors are light-emitting materials with stable optical properties that represent promising tools for bioimaging. The synthesis of nanophosphors, and thus the control of their surface properties, is, however, challenging. Here, flame aerosol technology is exploited to generate Tb-activated Y$_2$O$_3$ nanophosphors ($\sim$25 nm) encapsulated *in situ* by a nanothin amorphous inert SiO$_2$ film. The nanocrystalline core exhibits a bright green luminescence following the Tb^{3+} ion transitions, while the hermetic SiO$_2$-coating prevents any unspecific interference with cellular activities. The SiO$_2$-coated nanophosphors display minimal photobleaching upon imaging and can be easily functionalized through surface absorption of biological molecules. Therefore, they can be used as bionanoprobes for cell detection and for long-term monitoring of cellular activities. As an example, we report on the interaction between epidermal growth factor (EGF)-functionalized nanophosphors and mouse melanoma cells. The cellular uptake of the nanophosphors is visualized with confocal microscopy, and the specific activation of EGF receptors is revealed with biochemical techniques. Altogether, our results establish SiO$_2$-coated Tb-activated Y$_2$O$_3$ nanophosphors as superior imaging tools for biological applications.

KEYWORDS: bioimaging · nanoparticles · photobleaching · phosphorescence · epidermal growth factor

opened the way to the formation of crystalline nonaggregated[11] Y$_2$O$_3$ nanophosphors with uniform size and the desired crystallinity (cubic and monoclinic) in a single step and without any post heat treatment. Additionally, the emission wavelength of such phosphors can be fine-tuned from blue/green to red by co-doping the Y$_2$O$_3$ nanocrystals with Tb^{3+} and Eu^{3+} ions.[15]

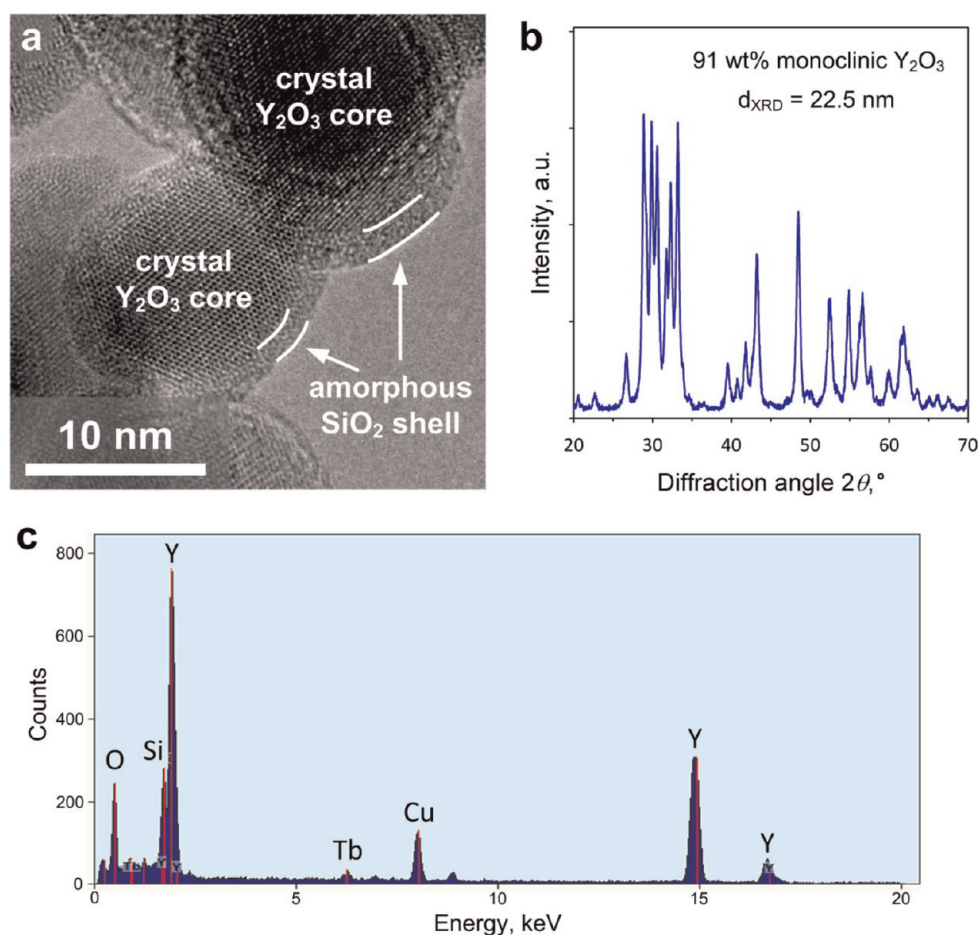The application of nanophosphors to bioimaging has been investigated with

Figure 1. (a) High-resolution transmission electron microscopy image of SiO_2-coated Y_2O_3:Tb^{3+} (4 at. %) nanophosphors. The crystal core is encapsulated by an amorphous hermetic nanothin SiO_2 film, indicated by white arrows. (b) X-ray diffraction analysis of the same sample, showing the characteristic pattern of the Y_2O_3 monoclinic phase with its corresponding weight fraction and average crystal size. (c) Elemental composition of a large area of the SiO_2-coated Y_2O_3:Tb^{3+} nanophosphors, which is verified by the presence of the Y, Tb, and Si peaks. The Cu peak comes from the copper grid used for the electron microscopy analysis.

promising results, for example, targeting specific channels on cell membranes by functionalizing the surface of YVO_4:Eu^{3+} nanoparticles[16] or detecting H_2O_2 concentration in living cells.[17] A few studies explored the synthesis of nanophosphor structures and their internalization by nonspecific phagocytosis upon incubation with cells.[10,18−20] Recently, the detection of cancer cells was demonstrated by the selective membrane binding of folic acid-functionalized Y_2O_3:Eu^{3+} nanoparticles.[9] These nanophosphors proved viable when incubated with fibroblasts, in sharp contrast to the strong cytotoxicity elicited by CdS QDs.[9] However, the majority of these toxicity studies was limited to a general analysis of cell viability and neglected potential effects on specific cell activities. Indeed, the interaction with nanoparticles, even at low concentration, may interfere with complex cellular functions such as differentiation or polarization.[21,22] In order to prevent such effects, an inert coating can be applied to the nanoparticle surface. As recently shown with nanosilver[23] and multifunctional plasmonic-magnetic nanostructures,[24]

this treatment minimizes the transport of toxic ions or direct contact with the cell[25] and, at the same time, improves the biocompatibility and dispersion in aqueous solutions.

Here, we report the synthesis of SiO_2-coated Y_2O_3:Tb^{3+} nanophosphors by scalable flame aerosol technology. The core nanocrystals are dry-coated *in situ* by a dense amorphous SiO_2 layer. The morphology and optical properties of the as-prepared SiO_2-coated nanophosphors are investigated by electron microscopy, X-ray analysis, 2-propanol chemisorption, and photoluminescent spectroscopy. The protective effect of the SiO_2 coating is revealed by monitoring neuronal differentiation of nerve growth factor stimulated PC12 cells.[22] Finally, the performance and optical stability of the as-prepared nanophosphors are tested by functionalizing their inert surface with epidermal growth factor (EGF)[26] and incubating them with mouse melanoma cells expressing high levels of the corresponding receptor (EGF receptor; EGFR) on the cell membrane. The internalization of EGF-functionalized nanophosphors is visualized with confocal microscopy, and the

specific activation of the EGFR is revealed with biochemical techniques. Altogether, our results establish SiO_2-coated Y_2O_3:Tb^{3+} nanophosphors as biocompatible and optically superior imaging probes for biomedical applications.

RESULTS AND DISCUSSION

Morphology: Crystal Structure and Coating Quality. Figure 1a shows a high-resolution electron microscopy image of the SiO_2-coated Y_2O_3:Tb^{3+} (4 at. % Tb-content) nanophosphor particles. The crystal Y_2O_3:Tb^{3+} core can be easily distinguished by the amorphous SiO_2 coating, which is hermetically encapsulating it with about 2 nm thickness.[27] This morphology is similar to other flame-made SiO_2-coated nanoparticles such as TiO_2,[27] super-paramagnetic Fe_2O_3,[28] Ag,[23] and multifunctional Janus-like Ag/Fe_2O_3.[24] The amorphous SiO_2 shell was deposited on the surface of the freshly formed core crystalline Y_2O_3:Tb^{3+} nanoparticles in a single step by swirl injection of the Si-precursor vapor[29] in contrast to SiO_2 shells made by wet chemistry. Dense, inert coatings are advantageous for biological applications, as they are biocompatible, minimize flocculation when dispersed in solutions (see Supporting Information, Figure S1), and, importantly, facilitate biofunctionalization of the surface.[23,24]

The crystallinity of the as-prepared nanophosphors was investigated by X-ray diffraction (XRD). Figure 1b shows the XRD spectrum of the SiO_2-coated Y_2O_3:Tb^{3+}. The peaks correspond mainly to the monoclinic Y_2O_3 crystal phase.[30] The monoclinic weight fraction in the core Y_2O_3 nanocrystals is about 91 wt %, as calculated by the Rietveld method, and its corresponding average crystal size is d_{XRD} = 22.5 nm, while the remaining 9 wt % corresponds to the cubic Y_2O_3 crystal phase. The presence of the amorphous nanothin SiO_2 coating did not influence the crystallinity nor the size of the core Y_2O_3:Tb^{3+} particles,[24,27,28] as the XRD spectrum was identical to that of pure core nanoparticles. The metastable monoclinic Y_2O_3 crystal phase can be obtained in high-temperature processes with fast cooling rates, such as flame spray pyrolysis.[11]

Figure 1c shows the elemental composition of a large area from the electron microscopy analysis. The visible peaks correspond to Y, O, and Tb, confirming their presence,[15] as well as Si from the SiO_2 coating. The peak corresponding to Cu comes from the copper grid used for the electron microscopy analysis. This indicates that no other impurities in the as-prepared nanophosphors were present, in agreement with other flame-made products.[31] Such impurity-free nanoparticles are especially desired for biological applications, in which any interaction with the biological system or adverse effect needs to be avoided.

The SiO_2 coating quality was evaluated by 2-propanol chemisorption.[32] 2-Propanol chemisorbs on the nanoparticle surface at 110 °C. The particles are then continuously heated to 500 °C in helium, and the
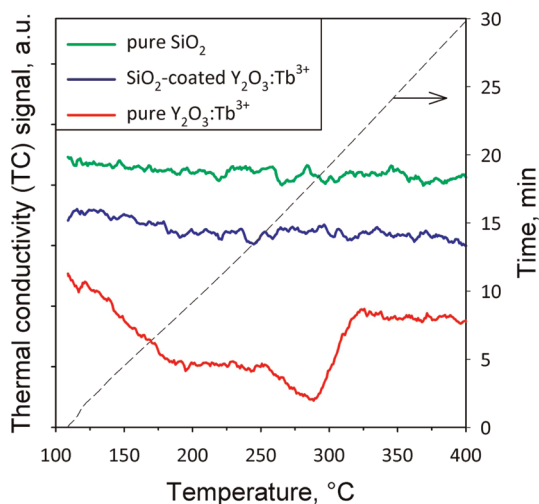

Figure 2. Thermal conductivity (TC) signal as a function of temperature (and time on the right ordinate, dashed black curve) during 2-propanol desorption and decomposition on pure Y_2O_3:Tb^{3+}, SiO_2-coated, and pure SiO_2. For the pure Y_2O_3:Tb^{3+} the TC decrease with temperature indicates the reaction of the Y_2O_3 surface. In contrast, the behavior of SiO_2-coated nanophosphors is similar to the pure SiO_2 without any TC decrease, indicating that the core particles are hermetically encapsulated by a SiO_2 layer.

thermal conductivity of the off-gases is monitored. 2-Propanol reacts on the surface, giving products (e.g., acetone or propene[33]) that evaporate from the particle and reducing the TC.[28,32] Figure 2 shows the TC signal of the off-gases as a function of temperature for pure Y_2O_3:Tb^{3+}, SiO_2-coated Y_2O_3:Tb^{3+}, and pure SiO_2 nanoparticles. For the pure Y_2O_3:Tb^{3+}, a decrease in the TC signal occurred at 200−300 °C with a minimum value around 280 °C. This temperature is close to the surface isopropoxide decomposition temperature for pure Y_2O_3 (240 °C).[33] Its slightly higher value might be attributed to the presence of the dopant Tb^{3+} (4 at. %), as it may also occupy some surface sites on the Y_2O_3 nanocrystals in line with the large surface-to-volume ratio.

In contrast, the TC signal of the SiO_2-coated Y_2O_3:Tb^{3+} was constant over the tested temperature range, indicating that no gas desorption from the nanoparticle surface took place.[32] The same behavior was observed for the pure SiO_2 nanoparticles and can be attributed to the significantly lower active surface site density for isopropoxide species on SiO_2 (0.5 μmol/m^2) than on Y_2O_3 (3.1 μmol/m^2).[33] All above results were verified by analyzing the mass spectrometry (MS) signal of the off-gases monitoring propene ($m/z = 41$), 2-propanol ($m/z = 41$, 43, and 45), and water ($m/z = 18$).[32] This indicates that the SiO_2 surface layer is hermetically encapsulating the core nanocrystals, in agreement with similarly dry-coated TiO_2 and Fe_2O_3 nanoparticles.[28,32] It should be noted that SiO_2 coatings obtained by wet chemistry are typically porous, allowing thus transport of ions through the SiO_2 shells.[34] In contrast, the SiO_2 nanothin coatings
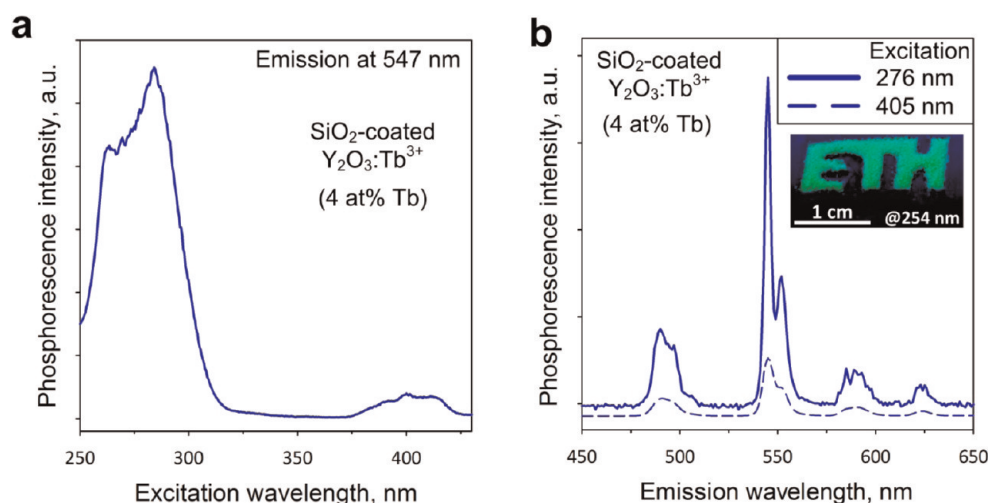
Figure 3. Optical properties of the SiO_2-coated $Y_2O_3:Tb^{3+}$ nanophosphors. (a) Excitation spectrum monitoring the emission at 547 nm. (b) Emission spectra upon excitation at 276 nm (solid blue line) or 405 nm (dashed blue line). The strongest emission peak is at 547 nm, corresponding to bright green color, as seen also in the inset (image obtained under excitation at 254 nm).

obtained here are dense and *hermetic*, thus inhibiting such ion transport.[24]

Optical Properties: Phosphorescence. Figure 3a displays the excitation spectrum of the SiO_2-coated $Y_2O_3:Tb^{3+}$ (4 at. %) nanophosphors monitoring the peak emission wavelength corresponding to the Tb^{3+} ion transitions at 547 nm. A strong band is located around 280 nm,[35] which is attributed to the Tb^{3+} ion transitions within the nanocrystals.[36] Despite the fact that the nanoparticle excitation peaks in this region, the irradiation of biological samples with high-energy wavelengths is not applicable to standard imaging, as it induces photodamage to biological samples. Importantly, a second absorption band peaks in the visible region and is centered at 400 nm. Such excitation wavelength is suitable for common bioimaging applications and is compatible with commercial microscope optics.

The emission spectra of the same nanophosphors for the excitation at 276 nm or at 405 nm are shown in Figure 3b. Both spectra display a sharp emission peak around 550 nm (Figure 3b, inset), which is attributed to the $^5D_4 \rightarrow {}^7F_5$ Tb^{3+} ion transitions.[37] The second strongest peak is located at 490 nm and is attributed to the $^5D_4 \rightarrow {}^7F_6$ Tb^{3+} ion transitions.[37] It should be noted that the position of the emission peaks in rare earth ion activated nanophosphors strongly depends on the chosen dopant element. For this reason, the SiO_2-coated nanophosphors have emission spectra similar to other Tb^{3+}-doped nanocrystals (*e.g.*, Gd_2O_3, $CePO_4$).[10,38]

Cytotoxicity: Biocompatible SiO_2 Coating. Rare earth activated nanophosphors do not significantly alter cell viability or proliferation when applied to biological systems, in contrast to other light-emitting nanoparticles that contain heavy metals (*e.g.*, quantum dots).[6] In order to evaluate the potential interference with more
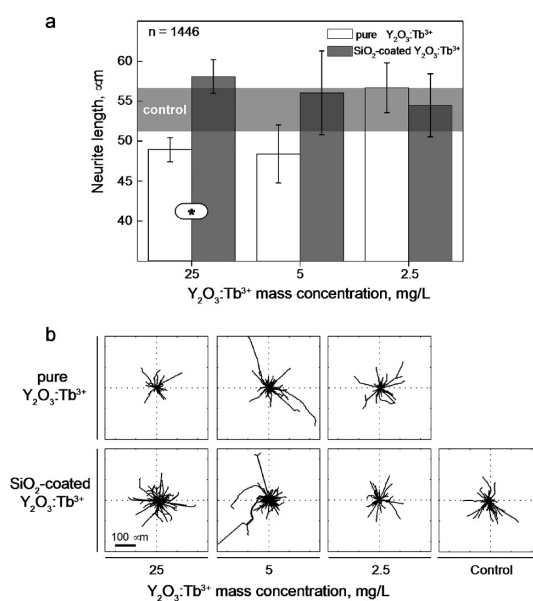

Figure 4. $Y_2O_3:Tb^{3+}$ nanophosphors' interference with neuronal differentiation. (a) Length of neurites generated after 6 days of stimulation with nerve growth factor by PC12 cells incubated with increasing concentrations of pure or SiO_2-coated $Y_2O_3:Tb^{3+}$ nanophosphors. The length of neurites generated by control cells is shown as a gray-shaded area. The number of measured neurites is reported in the upper left corner of the graph. Significant differences between the population means are reported (* indicates $p < 0.05$). Error bars represent the measured standard error of the mean. (b) Length and orientation of neurites generated by PC12 cells in the tested experimental conditions. The black lines in the diagrams correspond to individual neurite profiles.

specialized cellular activities, such as cell differentiation and polarization, we monitored[22] the effect of nanophosphors in a sensitive assay based on the neuronal differentiation of PC12 cells upon stimulation with nerve growth factor (NGF).[39] Unstimulated PC12 cells were preconditioned by 24 h incubation with increasing concentrations of pure or SiO_2-coated
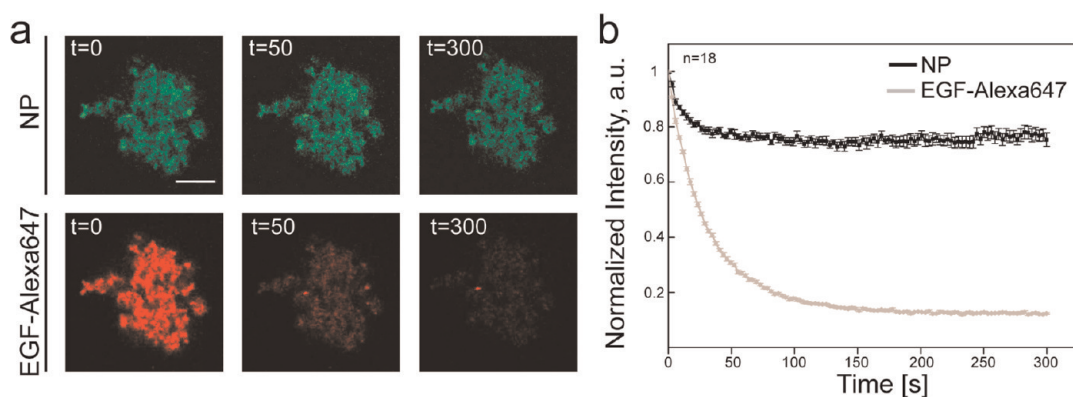
Figure 5. Optical stability of Y_2O_3:Tb^{3+} nanophosphors. (a) Photobleaching of EGF-Alexa 647-functionalized nanophosphors under continuous laser excitation in a confocal microscopy setup. The panels in the upper row display the emission from a large agglomerated structure of nanophosphors (NP) upon excitation with the 405 nm line of a solid-state laser, while the lower row displays the corresponding red emission from Alexa647 (EGF-Alexa 647) upon excitation with the 633 nm line of a HeNe laser. The corresponding time (expressed in seconds) is reported in the upper left corner of each panel. The scale bar is 10 μm. (b) Signal intensity curves obtained from photobleaching experiments. The intensity of the nanophosphor emission, normalized to the value at $t = 0$, is reported as a black line, while the corresponding intensity of Alexa647 emission is reported as a gray line. The number of averaged experiments is reported in the upper left corner of the graph. Error bars represent the standard error of the mean.

Y_2O_3:Tb^{3+} nanophosphors. The graph in Figure 4a shows the average length of neurites (i.e., the long cellular protrusions emanating from the cell body of developing neurons) generated by PC12 cells after 6 days of stimulation with NGF. The neurite length in the untreated control sample is shown as a shaded area, for comparison. For the pure Y_2O_3:Tb^{3+}, nanoparticle concentration as low as 25 mg/L (ppm) significantly reduced the neurite growth, indicating that even concentrations in the ppm level influence the delicate molecular pathways controlling neuronal differentiation. Importantly, at these concentrations no significant change in the overall cell viability was detected, as already reported by others.[9,10,18] At lower nanoparticle concentrations, the neurite length reached values similar to the control ones, especially for a concentration of 2.5 mg/L and below. In contrast, the length of neurites generated by cells incubated with the SiO_2-coated Y_2O_3:Tb^{3+} nanophosphors was similar to the control at all concentrations (Figure 4a). Figure 4b provides a visual representation of the length and orientation of neurites generated by PC12 cells incubated with nanoparticles. Importantly, in the presence of the SiO_2-coated nanophosphors, cells generated a bigger number of longer neurites, which extended randomly from the cell body. These results demonstrate that the SiO_2 coating eliminates the unspecific interference of nanophosphors with biological activities even at high concentrations, thus opening the door to their use in bioimaging applications.

Bioimaging: Optical Stability of Functionalized Nanophosphors. In order to demonstrate the suitability of the SiO_2-coated nanophosphors as highly specific bioimaging probes, we investigated the interaction of epidermal growth factor with its specific receptor in VE11 mouse melanoma cells.[40] EGF signaling was recently shown to be a delicate pathway, which is subject to unspecific disturbances by nanoparticles and can even be exploited for targeted tumor treatment by hyperthermia.[41] VE11 cells were selected because they express high levels of the EGFR (see Supporting Information, Figure S2), as common in many mammalian tumors.[42] The surface functionalization of the probes was obtained by direct incubation of the SiO_2-coated nanoparticles with fluorescently labeled EGF (EGF-Alexa647). Various proteins were shown to readily attach on the SiO_2 surface through physical adsorption based on van der Waals and electrostatic forces.[43,44] Covalent binding of EGF on the nanoparticle surface is also possible by appropriate additional surface functionalization steps.[26,41] A 100 mg/L solution of SiO_2-coated nanophosphors was mixed with 200 mg/L of a (1:1) solution of EGF-Alexa647 and EGF for 30 min, and the nanoparticles were then washed several times to remove the unbound EGF. This procedure yielded doubly labeled nanoparticles showing a green signal corresponding to the inherent nanoparticle phosphorescence and a red signal corresponding to the Alexa647 fluorescent emission (Figure 5a).

We subsequently investigated the optical stability of the EGF-functionalized nanophosphors by comparing the photobleaching rate of their two emissions upon laser excitation in a confocal microscopy setup (Figure 5a and b). Continuous excitation of Alexa647 with the 633 nm wavelength of a HeNe laser led to a drop of the red emission to a plateau dark value within 300 s (Figure 5b). Importantly, upon excitation with the 405 nm wavelength of a solid-state laser, the green emission from the agglomerated nanophosphors displayed limited bleaching, rapidly dropping to a plateau value corresponding to 75% of the initial intensity (Figure 5b). This slight decrease might be attributed
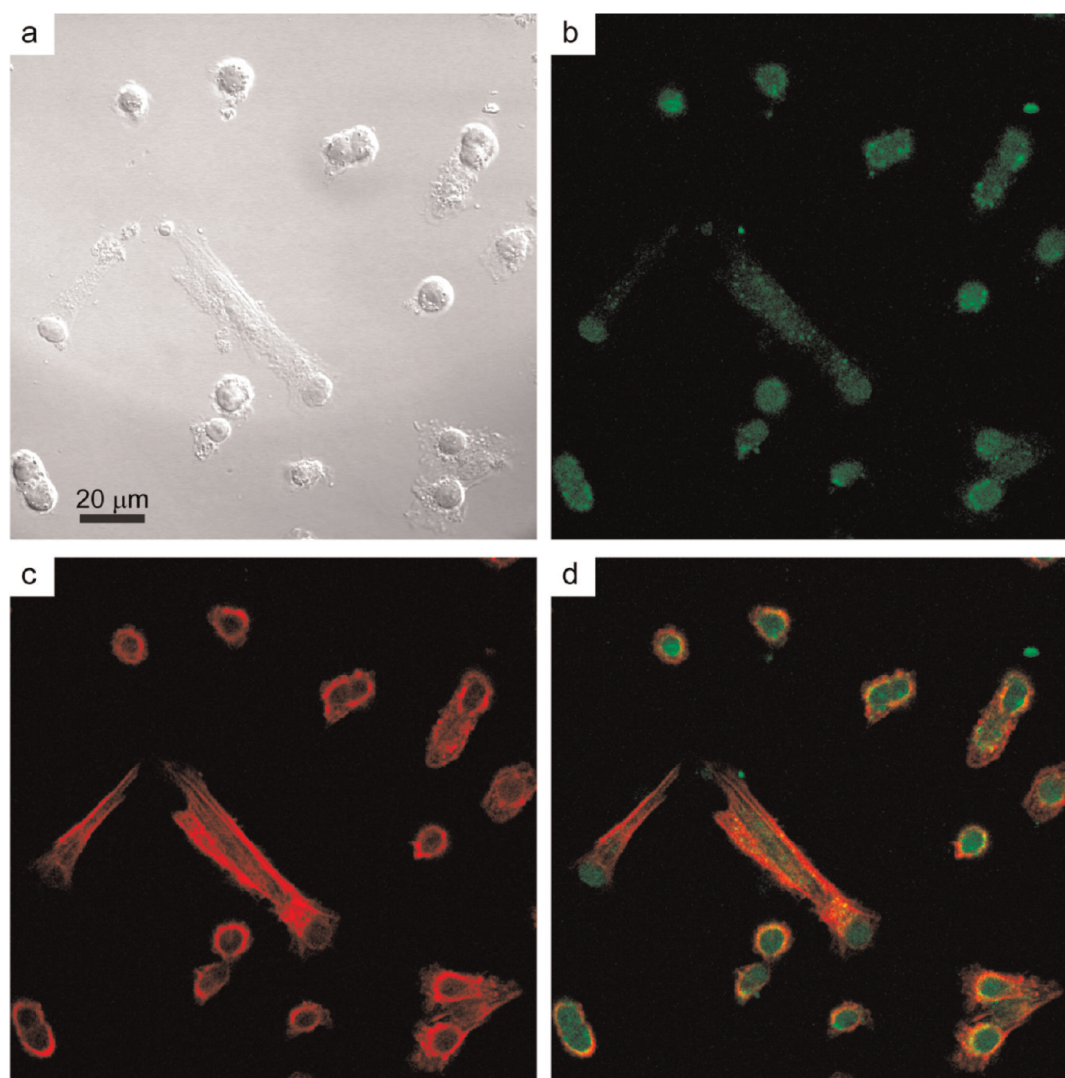
Figure 6. Uptake of EGF-functionalized Y_2O_3:Tb^{3+} nanophosphors by VE11 mouse melanoma cells. VE11 cells were incubated for 4 h with EGF-functionalized nanoparticles and then fixed and stained with FITC-phalloidin to reveal the actin cytoskeleton. (a) Differential interference contrast (DIC) image of VE11 mouse melanoma cells after 4 h of incubation with EGF-functionalized Y_2O_3:Tb^{3+} nanophosphors. (b) Confocal image of the nanophosphor emission and (c) the actin cytoskeleton. (d) Merged image of panels (b) and (c).

to the laser irradiation, as this could change the crystallinity of the nanophosphors or could induce the relocation of the Tb^{3+} to optically inactive clusters.[45] However, these results demonstrate the superior optical stability of the phosphorescent emission and the possibility to easily functionalize the nanoparticle surface with fluorescently labeled bioactive molecules.

Bioimaging: Specific Activation of EGFR in Melanoma Cells. Figure 6 shows representative confocal images of the particle internalization by VE11 melanoma cells (Figure 6a). EGF-functionalized nanoparticles were readily internalized by cells after 4 h incubation, as demonstrated by the presence of the dotted green signal (Figure 6b) close to the cortical actin ring[46] (Figure 6c) or inside it (Figure 6d), indicating that the inherent phosphorescent properties are retained upon cellular uptake.[10] These results suggest that the interaction between melanoma cells and nanophosphors is

most probably governed by the specific binding between EGF and its membrane receptor,[26] which is then followed by a binding-triggered internalization step. However, it cannot be excluded that unspecific mechanisms, such as micropinocytosis, contribute to the internalization of EGF-conjugated nanoparticles.

In order to further confirm the specificity and efficiency of the interaction between EGF-functionalized nanoparticles and melanoma cells, we directly measured the EGFR activation in a Western blot assay (Figure 7a). Binding of EGFR to its ligand induces the phosphorylation of a cytoplasmic residue (Tyr1068) and initiates a signaling cascade within the cell.[47] The Western blot results reported in Figure 7b show that the level of EGFR phosphorylation (pEGFR) induced by the incubation of cells with EGF-functionalized nanophosphors was comparable to that obtained by direct incubation with a 500 ng/mL solution of EGF. It is worth
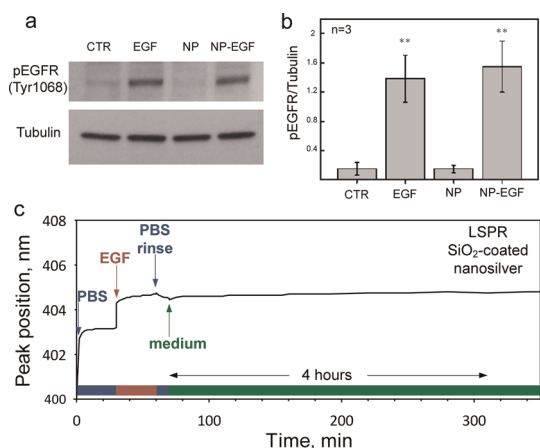
Figure 7. Western blot analysis of EGFR activation in VE11 mouse melanoma cells by EGF-functionalized Y_2O_3:Tb^{3+} nanophosphors. (a) The activation of EGFR is revealed through the quantification of EGFR phosphorylation in Tyr1068 (upper band) relative to the loading control (lower band). (b) Quantification of Western blot band intensity from three independent experiments. Significant differences between the population means and the control are reported (** indicates $p < 0.01$). (c) Time evolution of the plasmon peak position of a localized surface plasmon resonance (LSPR) biosensor with SiO_2-coated nanosilver[23] mounted on a flow-cell. Initially, the biosensor signal is stabilized in the presence of the buffer solution (PBS). Then, the EGF-containing solution is injected, shifting the peak position to higher wavelength. This shift is maintained after the rinsing with buffer (PBS rinse) and incubation with cell medium (medium) for a period of over 4 h.

noting that nonfunctionalized nanoparticles did not induce receptor activation, and the corresponding level of EGFR phosphorylation was similar to that measured in control, nontreated cells (Figure 7a,b). However, they were also internalized upon incubation with cells, as typically observed for other nanoparticles.[10,18,48] Therefore, all the above results demonstrate the possibility to use the SiO_2-coated nanophosphors as biological probes to bind and activate selected membrane receptors in living cells.

The protein layer stability on the surface of our SiO_2-coated nanophosphors was investigated with a localized surface plasmon resonance (LSPR) biosensor with identically SiO_2-coated nanosilver.[23] The plasmonic extinction band of such SiO_2-coated silver nanoparticles depends on the refractive index of the medium surrounding them.[49] The refractive index of the proteins is higher than that of buffer solutions, so upon physical adsorption of the former on the SiO_2 coating, the extinction band undergoes a red shift. Figure 7c shows the peak position wavelength of SiO_2-coated nanosilver of about 30 nm diameter monitored over time, *in situ* mounted on a flow-cell.[23] Initially (at time = 0−30 min), the signal stabilizes in the presence of PBS buffer solution. Then, the EGF-containing solution is injected (at time = 30 min), whereupon a sharp increase is observed. This increase indicates that the EGF is adsorbed on the SiO_2 surface. After a few minutes the

signal stabilizes again, indicating the end of the EGF-SiO_2 coating interaction. A rinsing step with PBS follows, during which the plasmon band shift remains constant. This indicates that the EGF is stable on the SiO_2 coating. Afterward, cell medium is injected in the flow-cell, again without any further change in the plasmon band for over 4 h. Therefore, the EGF biofunctionalization of the SiO_2 coating is stable upon rinsing and incubation with the cell growth medium for several hours, and such biofunctionalization should be performed on the same day of the cell experiments.

CONCLUSIONS

SiO_2-coated Y_2O_3:Tb^{3+} nanophosphors were generated by a scalable flame aerosol technology. The as-prepared nanoparticles exhibited a high crystalline monoclinic Y_2O_3 core encapsulated by a nanothin, dense, amorphous SiO_2 layer (Figure 1). The core is responsible for the resulting phosphorescence, and the nanophosphors exhibited the characteristic bands attributed to the Tb^{3+} ion transitions, yielding bright emission peaks in the green region of the visible spectrum (Figure 3). In particular, when compared to the fluorescent emission of a commercial organic dye (Alexa647), the inherent nanophosphor emission proved virtually photobleaching-free (Figure 5), as more than 75% of the initial signal was retained under continuous laser excitation. The limited photobleaching effect can be ascribed to the inherent nanophosphor photostability. Additionally, the phosphorescent properties were not lost upon uptake by melanoma cells, thus allowing the detection of cellular internalization (Figure 6).

Such nanophosphors can be fully encapsulated hermetically by a nanothin homogeneous SiO_2 layer, as confirmed by 2-propanol chemisorption (Figure 2). The relevance of this coating is 2-fold: First, it minimizes the unspecific interference of the nanoparticles with cellular activities. Second, it provides a substrate for the facile functionalization of the nanophosphor surface. Even though the relative cytotoxicity of Y_2O_3 nanoparticles, especially when compared to quantum dots, is very low, the interference with delicate cellular processes, such as neuronal differentiation or EGF signaling,[21,22] may severely limit their use as biological nanoprobes. Indeed, the pure Y_2O_3:Tb^{3+} nanophosphors hindered neurite generation by PC12 cells even at low concentrations (Figure 4). This effect may be caused by the interaction of the crystalline Y_2O_3 nanoparticles with the cell membrane or by their ion release. The presence of a SiO_2 coating completely abolished any unspecific interference, and neuronal differentiation, a process highly sensitive to nanoparticle toxicity, proceeded as in control, untreated cells.

Additionally, the SiO_2 layer allowed a stable functionalization of the inert nanoparticle surface through a simple incubation step. Using this protocol we obtained EGF-functionalized nanophosphors

that readily interacted with melanoma cells through the binding and activation of the specific EGF receptor (Figures 6 and 7). However, this technology can be applied virtually to any soluble mitogen or biologically active molecule, thus targeting the nanophosphor to selected receptors on the plasma membrane.

In conclusion, the scalable flame aerosol synthesis of biocompatible Y_2O_3:Tb^{3+} nanophosphors and their *in situ* coating by a nanothin SiO_2 layer in a single step enables them to be effectively employed in bioimaging for dynamic monitoring of cell functions that may help clarify specific biological pathways.

METHODS

Synthesis and Characterization of SiO_2-Coated Y_2O_3:Tb^{3+} Nanoparticles. SiO_2-coated monoclinic Y_2O_3:Tb^{3+} nanophosphors were generated using a modified enclosed FSP reactor.[27] In brief, yttrium nitrate (Aldrich, 99.9%) was dissolved in a 1:1 by volume mixture of 2-ethylhexanoic acid (Riedel-de Haen, 99%) and ethanol (Alcosuisse) to form the precursor solution. The molarity was kept constant at 0.5 M for Y metal. The Tb doping was achieved by adding 4 at. % Tb nitrate (Aldrich, 99.9%) to the above solution. The Tb atomic fraction (at. %) was defined with respect to the total metal ion concentration. The precursor solution was fed at the FSP nozzle (5 mL/min) and dispersed by 5 L/min oxygen (PanGas, purity >99.9%) and sheathed by 40 L/min oxygen. The freshly formed core Y_2O_3:Tb^{3+} particles were coated in-flight by swirl injection of hexamethyldisiloxane (HMDSO, Sigma Aldrich, purity ≥99%) vapor with 15 L/min nitrogen (PanGas, purity >99.9%) at room temperature through a metallic ring with 16 equidistant openings. The ring was placed on top of a 20 cm long quartz glass tube (inner diameter 4.5 cm) followed by another 30 cm long such tube. The HMDSO vapor was supplied by bubbling nitrogen through approximately 350 mL of liquid HMDSO in a 500 mL glass flask. The SiO_2 amount was kept constant in the product particles and was calculated at saturation conditions (bubbler temperature 9 °C and 0.5 L/min N_2), corresponding to 16.6 wt %. The as-prepared nanophosphor particles were collected on a glass microfiber filter (Whatman GF6, 257 mm diameter). Uncoated monoclinic Y_2O_3:Tb^{3+} particles were made at identical conditions as above in the absence, however, of the HMDSO vapor.

X-ray diffraction patterns were recorded by a Bruker AXS D8 Advance diffractometer (40 kV, 40 mA, Cu Kα radiation) at 2θ = 20−70° with a step size of 0.03°. The obtained spectra were fitted using the TOPAS 3 software (Bruker) and the Rietveld fundamental parameter refinement.[11] High-resolution transmission electron microscopy (HR-TEM) was performed with a CM30ST microscope (FEI; LaB6 cathode, operated at 300 kV, point resolution ∼2 Å). Product particles were dispersed in ethanol and deposited onto a perforated carbon foil supported on a copper grid. The photoluminescence of the particles was characterized at room temperature using a fluorescence spectrophotometer (Varian Cary Eclipse) containing a Xe flash lamp with tunable emission wavelength. Samples of 30 mg were filled in a cylindrical substrate holder of 10 mm diameter and pressed toward a quartz glass front window. Emission spectra were recorded from 450 to 650 nm; excitation spectra, from 200 to 400 nm with a step size of 0.5 nm. The chemisorption of 2-propanol on FSP-made particles was performed following Teleki et al.[32] on a Micromeritics Autochem II 2920 unit. Prior to these experiments, samples (50 mg each) were heated at 10 °C/min to 400 °C and kept there for 30 min in a 20% O_2 in Ar atmosphere (50 mL/min) to remove surface water and carbonaceous species. The sample was then cooled to 110 °C and flushed with He for 10 min. 2-Propanol (2000 ppm; Messer) in N_2 (50 mL/min) was then introduced at 110 °C for 30 min to minimize physisorption and optimize chemisorption of 2-propanol. The gas atmosphere was again changed to He, and after 10 min the sample was heated at 10 °C/min to 500 °C. During this final heating stage the thermal conductivity of the off-gases was monitored by a thermal conductivity detector in the Autochem. The off-gases from the Autochem were analyzed by a mass spectrometer (Thermo Star, Pfeiffer Vacuum, SEM and

emission mode). The masses m/z = 45, 43, and 41 were measured for desorbed unreacted 2-propanol, m/z = 41 for propene formed and m/z = 18 for water released.

Cytotoxicity Assay. PC12 cells were grown in RPMI-1640 medium (Sigma-Aldrich, USA) supplemented with 10% v/v fetal bovine serum, 2 mM L-glutamine, 100 U/mL penicillin, and 100 µg/mL streptomycin (all from Sigma-Aldrich, USA) and maintained at 37 °C and 5% of CO_2. For the cytotoxicity assay, commercial cell culture plates were incubated with 1% gelatin for 1 h at room temperature (RT) and then with a 2% glutaraldehyde solution in PBS for 15 min at RT. The glutaraldehyde solution was then removed and replaced with a 70% solution of ethanol in PBS for 1 h at RT. The substrates were washed five times with PBS (5 min each) and then incubated overnight with a 2 mM glycine solution in PBS. The plates were finally washed five times (5 min each) with PBS. Low-passage PC12 cells were gently detached from subconfluent cultures and left to sediment in a 15 mL tube for 15 min at 37 °C and 5% of CO_2. Single cells obtained from the supernatant were counted and seeded in gelatin-coated 12-well plates to a final density of 3×10^4 cells/well. The cells were initially incubated for 24 h to allow proper adhesion to the substrate. The pure and SiO_2-coated Y_2O_3:Tb^{3+} nanoparticles were dispersed in PBS at Y_2O_3:Tb^{3+} mass concentration of 50 mg/L by ultrasonication (Sonics Vibra cell, 5 min, 0.5/0.5 s, 75%). The nanoparticle suspensions were then autoclaved, allowed to cool at RT, and further ultrasonicated in a bath for 30 min. Before adding the nanoparticles to the cells the cell culture medium was carefully removed and replaced with fresh complete medium. The cells were then incubated with the nanoparticles at different concentrations (Figure 4) for 24 h. The cultures were subsequently gently washed three times with PBS (5 min each), and new complete medium was added. After another incubation step of 24 h the complete medium was removed and replaced with induction medium (RPMI medium supplemented with 1% FBS, 5% HS) containing NGF (100 ng/mL).

Functionalization of SiO_2-Coated Nanophosphors. SiO_2-coated Y_2O_3:Tb^{3+} nanophosphors were dispersed in PBS at a final concentration of 100 mg/L. A 1 mL amount of this suspension was centrifuged for 2 min at 800 rpm and resuspended in 0.9 mL of PBS. A solution of reconstituted EGF (Sigma Aldrich, 200 mg/L) or EGF and EGF-Alexa647 (Life Technologies, 200 mg/L) in PBS was added to obtain a final volume of 1 mL. The nanophosphors were then incubated with EGF or EGF-Alexa647 for 30 min at 37 °C. Afterward, the suspension was centrifuged (2 min at 800 rpm) and resuspended in 1 mL of cell medium (without serum) three times. The stability of the EGF biofunctionalization on the SiO_2 surface was evaluated by employing a localized surface plasmon resonance biosensor with identically SiO_2-coated nanosilver particles.[23] In brief, the SiO_2-coated nanosilver particles of about 30 nm diameter were deposited on a glass substrate and mounted on a flow-cell. The optical properties of the plasmonic film could be *in situ* monitored on a Varian Cary 500 spectrophotometer for a wavelength range of 350−650 nm. The corresponding biological solutions were then injected in the flow-cell, and the peak position shift was monitored over time. The EGF-containing solution had a concentration of 20 mg/L. The plasmonic peak position was determined by polynomial fitting.

EGFR Activation in Mouse Melanoma Cells. VE11 mouse melanoma cells were grown in RPMI-1640 medium (Sigma-Aldrich, USA) supplemented with 10% v/v fetal bovine serum, 2 mM L-glutamine, 100 U/mL penicillin, and 100 µg/mL streptomycin

(all from Sigma-Aldrich, USA) and maintained at 37 °C and 5% CO_2. For the measure of EGFR activation, VE11 cells were seeded into a 5 cm Petri dish in serum-free medium to a final density of 2.5×10^4 cells/cm^2. After 24 h of incubation the medium was replaced with 5 mL of serum-free medium (control condition) or with 5 mL of serum-free medium supplemented with EGF (500 ng/mL), nonfunctionalized SiO_2-coated Y_2O_3:Tb^{3+} nanophosphors (33 mg/L), or EGF-functionalized SiO_2-coated Y_2O_3: Tb^{3+} nanophosphors (33 mg/L). After 20 min of incubation at 37 °C and 5% CO_2 the cell medium was removed and lysis buffer was directly added to the cells. After 5 min the cell lysates were collected by scraping, heated for 5 min at 95 °C, and then centrifuged and stored at −20 °C. Cell lysates were analyzed by standard Western blot using antibodies against (Tyr1068)-phosphorylated EGFR (#3777, Cell Signaling Technologies, USA) and tubulin (rabbit anti-tubulin; #T3526, Sigma).

For the visualization of EGF-functionalized nanophosphor uptake, VE11 cells were seeded into Lab-Tek chambered coverslips (Thermo Scientific, USA) to a final density of 1×10^4 cells/ cm^2. After 24 h incubation the medium was replaced with 3 mL of serum-free medium supplemented with EGF-functionalized SiO_2-coated Y_2O_3:Tb^{3+} nanophosphors (33 mg/L). After 4 h incubation the cells were fixed and permeabilized with a solution of 0.5% Triton X-100 in 3% PFA for 3 min at RT. Cells were then fixed again with 3% PFA for 15 min at RT. After rinsing three times for 5 min with PBS the cells were incubated for 1 h in blocking buffer (5% BSA in PBS). In order to stain F-actin, the cells were incubated with TRITC-Phalloidin (Sigma-Aldrich, USA), dilution 1:50 in 5% BSA in PBS, for 1 h at RT.

Total EGFR in VE11 mouse melanoma was detected incubating the cells overnight at 4 °C with primary anti-EGFR antibody (ab#2430, Abcam, UK). The cells were then incubated with secondary anti-rabbit antibody (Alexa 555, Molecular Probes, USA) for 45 min at RT. Nuclei were visualized using standard DAPI staining. At the end of the staining procedure the samples were rinsed three times for 5 min with PBS, mounted, and immediately imaged.

Microscopy and Image Analysis. Transmission images of neurites generated by NGF-stimulated PC12 cells were collected with a wide-field microscope (Nikon Ti PSF; Nikon, Japan) equipped with an Orca R-2 CCD camera (Hamamatsu Photonic, Japan) using a 20×, 0.45 NA long-distance objective (Plan Fluor, Nikon). Fluorescent wide-field images of VE11 melanoma cells stained with total EGFR antibodies were acquired with a 40×, 1.30 NA oil immersion objective (PlanFluor, Nikon) using a FITC filter to collect Alexa555 signals and a DAPI filter to visualize the nuclei.

Confocal images of melanoma cells incubated with EGF-functionalized nanophosphors were collected with a Leica SP2-FCS (Leica, Germany) using a 63×, 1.4 NA, oil immersion objective (Plan-Apo, Leica). The nanophosphor emission was excited with the 405 nm wavelength of a solid-state laser (absolute power 12 mW) and collected in the 450−600 nm optical window. The EGF-Alexa647 emission was excited with the 633 nm wavelength of a HeNe laser (absolute power 3 mW) and collected in the 650−800 nm optical window. In order to measure photobleaching of the nanophosphors and Alexa647 signals, the laser power was set to 80%, and time lapses were collected with Δt of 2 s for a total of 5 min. The FITC-phalloidin emission was excited with the 561 nm wavelength of a solid-state laser and collected in the 580−650 nm optical window.

For the analysis of neurite length in NGF-stimulated PC12 cells (Figure 4), collected images were loaded into ImageJ (National Institute of Health, USA) and analyzed using the NeuronJ plug-in. For the photobleaching analysis (Figure 5) collected movies were analyzed using the confocal software LCS Lite (Leica). A region of interest was defined around the nanoparticles using the freehand selection tool to obtain the mean value of the fluorescent channels. A second region of interest was selected outside of the nanoparticles to obtain the corresponding background levels. The data were then exported as text files and loaded in Origin Pro8G (Origin Lab, USA). Photobleaching curves were obtained subtracting the relative background from each fluorescent channel and normalizing the values to the intensity recorded at time 0. Curves obtained from different photobleaching movies were averaged to obtain the plot presented in Figure 5.

Statistical Analysis. Statistical comparison of average neurite length was performed using a nonparametric Mann−Whitney test ($\alpha = 0.05$). All quantitative measurements reported are expressed as average values ± the standard error of the mean. The total number of events counted is reported in the upper or lower right corner of the presented graphs.

REFERENCES AND NOTES

1. Project on Emerging Nanotechnologies. www.nano-techproject.org, October 2011.
2. Alivisatos, P. The Use of Nanocrystals in Biological Detection. *Nat. Biotechnol.* **2004**, *22*, 47–52.
3. Norris, D. J.; Efros, A. L.; Erwin, S. C. Doped Nanocrystals. *Science* **2008**, *319*, 1776–1779.
4. Erogbogbo, F.; Yong, K.-T.; Roy, I.; Xu, G.; Prasad, P. N.; Swihart, M. T. Biocompatible Luminescent Silicon Quantum Dots for Imaging of Cancer Cells. *ACS Nano* **2008**, *2*, 873–878.
5. Nirmal, M.; Dabbousi, B. O.; Bawendi, M. G.; Macklin, J. J.; Trautman, J. K.; Harris, T. D.; Brus, L. E. Fluorescence Intermittency in Single Cadmium Selenide Nanocrystals. *Nature* **1996**, *383*, 802–804.
6. Medintz, I. L.; Uyeda, H. T.; Goldman, E. R.; Mattoussi, H. Quantum Dot Bioconjugates for Imaging, Labelling and Sensing. *Nat. Mater.* **2005**, *4*, 435–446.
7. Rehberg, M.; Praetner, M.; Leite, C. F.; Reichel, C. A.; Bihari, P.; Mildner, K.; Duhr, S.; Zeuschner, D.; Krombach, F. Quantum Dots Modulate Leukocyte Adhesion and Transmigration Depending on Their Surface Modification. *Nano Lett.* **2010**, *10*, 3656–3664.
8. Feldmann, C.; Justel, T.; Ronda, C. R.; Schmidt, P. J. Inorganic Luminescent Materials: 100 Years of Research and Application. *Adv. Funct. Mater.* **2003**, *13*, 511–516.
9. Setua, S.; Menon, D.; Asok, A.; Nair, S.; Koyakutty, M. Folate Receptor Targeted, Rare-Earth Oxide Nanocrystals for Bi-Modal Fluorescence and Magnetic Imaging of Cancer Cells. *Biomaterials* **2010**, *31*, 714–729.
10. Zhang, F.; Wong, S. S. Ambient Large-Scale Template-Mediated Synthesis of High-Aspect Ratio Single-Crystalline, Chemically Doped Rare-Earth Phosphate Nanowires for Bioimaging. *ACS Nano* **2010**, *4*, 99–112.
11. Camenzind, A.; Strobel, R.; Pratsinis, S. E. Cubic or Monoclinic Y_2O_3:Eu^{3+} Nanoparticles by One Step Flame Spray Pyrolysis. *Chem. Phys. Lett.* **2005**, *415*, 193–197.
12. Camenzind, A.; Strobel, R.; Krumeich, F.; Pratsinis, S. E. Luminescence and Crystallinity of Flame-Made Y_2O_3: Eu^{3+} Nanoparticles. *Adv. Powder Technol.* **2007**, *18*, 5–22.
13. Mialon, G.; Gohin, M.; Gacoin, T.; Boilot, J. P. High Temperature Strategy for Oxide Nanoparticle Synthesis. *ACS Nano* **2008**, *2*, 2505–2512.
14. Pratsinis, S. E. Flame Aerosol Synthesis of Ceramic Powders. *Prog. Energy Combust. Sci.* **1998**, *24*, 197–219.
15. Sotiriou, G. A.; Schneider, M.; Pratsinis, S. E. Color-Tunable Nanophosphors by Codoping Flame-Made Y_2O_3 with Tb and Eu. *J. Phys. Chem. C* **2011**, *115*, 1084–1089.
16. Beaurepaire, E.; Buissette, V.; Sauviat, M. P.; Giaume, D.; Lahlil, K.; Mercuri, A.; Casanova, D.; Huignard, A.; Martin, J. L.; Gacoin, T.; *et al.* Functionalized Fluorescent Oxide Nanoparticles: Artificial Toxins for Sodium Channel Targeting and Imaging at the Single-Molecule Level. *Nano Lett.* **2004**, *4*, 2079–2083.

17. Casanova, D.; Bouzigues, C.; Nguyen, T. L.; Ramodiharilafy, R. O.; Bouzhir-Sima, L.; Gacoin, T.; Boilot, J. P.; Tharaux, P. L.; Alexandrou, A. Single Europium-Doped Nanoparticles Measure Temporal Pattern of Reactive Oxygen Species Production inside Cells. *Nat. Nanotechnol.* **2009**, *4*, 581–585.

18. Di, W. H.; Li, J.; Shirahata, N.; Sakka, Y.; Willinger, M. G.; Pinna, N. Photoluminescence, Cytotoxicity and *in Vitro* Imaging of Hexagonal Terbium Phosphate Nanoparticles Doped with Europium. *Nanoscale* **2011**, *3*, 1263–1269.

19. Gupta, B. K.; Rathee, V.; Narayanan, T. N.; Thanikaivelan, P.; Saha, A.; Govind; Singh, S. P.; Shanker, V.; Marti, A. A.; Ajayan, P. M. Probing a Bifunctional Luminomagnetic Nanophosphor for Biological Applications: A Photoluminescence and Time-Resolved Spectroscopic Study. *Small* **2011**, *7*, 1767–1773.

20. Lechevallier, S.; Lecante, P.; Mauricot, R.; Dexpert, H.; Dexpert-Ghys, J.; Kong, H. K.; Law, G. L.; Wong, K. L. Gadolinium-Europium Carbonate Particles: Controlled Precipitation for Luminescent Biolabeling. *Chem. Mater.* **2010**, *22*, 6153–6161.

21. Comfort, K. K.; Maurer, E. I.; Braydich-Stolle, L. K.; Hussain, S. M. Interference of Silver, Gold, and Iron Oxide Nanoparticles on Epidermal Growth Factor Signal Transduction in Epithelial Cells. *ACS Nano* **2011**, *5*, 10000–10008.

22. Soenen, S. J. H.; Himmelreich, U.; Nuytten, N.; Pisanic, T. R.; Ferrari, A.; De Cuyper, M. Intracellular Nanoparticle Coating Stability Determines Nanoparticle Diagnostics Efficacy and Cell Functionality. *Small* **2010**, *6*, 2136–2145.

23. Sotiriou, G. A.; Sannomiya, T.; Teleki, A.; Krumeich, F.; Vörös, J.; Pratsinis, S. E. Non-Toxic Dry-Coated Nanosilver for Plasmonic Biosensors. *Adv. Funct. Mater.* **2010**, *20*, 4250–4257.

24. Sotiriou, G. A.; Hirt, A. M.; Lozach, P. Y.; Teleki, A.; Krumeich, F.; Pratsinis, S. E. Hybrid, Silica-Coated, Janus-Like Plasmonic-Magnetic Nanoparticles. *Chem. Mater.* **2011**, *23*, 1985–1992.

25. Sotiriou, G. A.; Pratsinis, S. E. Antibacterial Activity of Nanosilver Ions and Particles. *Environ. Sci. Technol.* **2010**, *44*, 5649–5654.

26. Aaron, J.; Travis, K.; Harrison, N.; Sokolov, K. Dynamic Imaging of Molecular Assemblies in Live Cells Based on Nanoparticle Plasmon Resonance Coupling. *Nano Lett.* **2009**, *9*, 3612–3618.

27. Teleki, A.; Heine, M. C.; Krumeich, F.; Akhtar, M. K.; Pratsinis, S. E. *In Situ* Coating of Flame-Made TiO_2 Particles with Nanothin SiO_2 Films. *Langmuir* **2008**, *24*, 12553–12558.

28. Teleki, A.; Suter, M.; Kidambi, P. R.; Ergeneman, O.; Krumeich, F.; Nelson, B. J.; Pratsinis, S. E. Hermetically Coated Superparamagnetic Fe_2O_3 Particles with SiO_2 Nanofilms. *Chem. Mater.* **2009**, *21*, 2094–2100.

29. Teleki, A.; Buesser, B.; Heine, M. C.; Krumeich, F.; Akhtar, M. K.; Pratsinis, S. E. Role of Gas-Aerosol Mixing During *in Situ* Coating of Flame-Made Titania Particles. *Ind. Eng. Chem. Res.* **2009**, *48*, 85–92.

30. Sotiriou, G. A.; Schneider, M.; Pratsinis, S. E. Green, Silica-Coated Monoclinic Y_2O_3:Tb^{3+} Nanophosphors: Flame Synthesis and Characterization. *J. Phys. Chem. C* **2012**, *116*, 4493–4499.

31. Pratsinis, S. E.; Mastrangelo, S. V. R. Material Synthesis in Aerosol Reactors. *Chem. Eng. Prog.* **1989**, *85*, 62–66.

32. Teleki, A.; Akhtar, M. K.; Pratsinis, S. E. The Quality of SiO_2-Coatings on Flame-Made TiO_2-Based Nanoparticles. *J. Mater. Chem.* **2008**, *18*, 3547–3555.

33. Kulkarni, D.; Wachs, S. E. Isopropanol Oxidation by Pure Metal Oxide Catalysts: Number of Active Surface Sites and Turnover Frequencies. *Appl. Catal., A* **2002**, *237*, 121–137.

34. Aslan, K.; Wu, M.; Lakowicz, J. R.; Geddes, C. D. Fluorescent Core-Shell $Ag@SiO_2$ Nanocomposites for Metal-Enhanced Fluorescence and Single Nanoparticle Sensing Platforms. *J. Am. Chem. Soc.* **2007**, *129*, 1524–1525.

35. Das, G. K.; Tan, T. T. Y. Rare-Earth-Doped and Codoped Y_2O_3 Nanomaterials as Potential Bioimaging Probes. *J. Phys. Chem. C* **2008**, *112*, 11211–11217.

36. Meng, Q. Y.; Chen, B. J.; Xu, W.; Yang, Y. M.; Zhao, X. X.; Di, W. H.; Lu, S. Z.; Wang, X. J.; Sun, J. S.; Cheng, L. H.; *et al.* Size-Dependent Excitation Spectra and Energy Transfer in Tb^{3+}-Doped Y_2O_3 Nanocrystalline. *J. Appl. Phys.* **2007**, *102*, 093505.

37. Ray, S.; Patra, A.; Pramanik, P. Photoluminescence Properties of Nanocrystalline Tb^{3+} Doped Y_2O_3 Phosphor Prepared through a Novel Synthetic Route. *Opt. Mater.* **2007**, *30*, 608–616.

38. Gozzi, D.; Latini, A.; Salviati, G.; Armani, N. Growth and Characterization of Red-Green-Blue Cathodoluminescent Ceramic Films. *J. Appl. Phys.* **2006**, *99*, 123524.

39. Ferrari, A.; Cecchini, M.; Serresi, M.; Faraci, P.; Pisignano, D.; Beltram, F. Neuronal Polarity Selection by Topography-Induced Focal Adhesion Control. *Biomaterials* **2010**, *31*, 4682–4694.

40. Wellbrock, C.; Ogilvie, L.; Hedley, D.; Karasarides, M.; Martin, J.; Niculescu-Duvaz, D.; Springer, C. J.; Marais, R. ^{V599E}B-RAf Is an Oncogene in Melanocytes. *Cancer Res.* **2004**, *64*, 2338–2342.

41. Creixell, M.; Bohórquez, A. C.; Torres-Lugo, M.; Rinaldi, C. EGFR-Targeted Magnetic Nanoparticle Heaters Kill Cancer Cells without a Perceptible Temperature Rise. *ACS Nano* **2011**, *5*, 7124–7129.

42. Burke, P.; Schooler, K.; Wiley, H. S. Regulation of Epidermal Growth Factor Receptor Signaling by Endocytosis and Intracellular Trafficking. *Mol. Biol. Cell* **2001**, *12*, 1897–1910.

43. Roth, C. M.; Lenhoff, A. M. Electrostatic and Van der Waals Contributions to Protein Adsorption: Comparison of Theory and Experiment. *Langmuir* **1995**, *11*, 3500–3509.

44. Kenausis, G. L.; Voros, J.; Elbert, D. L.; Huang, N. P.; Hofer, R.; Ruiz-Taylor, L.; Textor, M.; Hubbell, J. A.; Spencer, N. D. Poly(L-Lysine)-G-Poly(Ethylene Glycol) Layers on Metal Oxide Surfaces: Attachment Mechanism and Effects of Polymer Architecture on Resistance to Protein Adsorption. *J. Phys. Chem. B* **2000**, *104*, 3298–3309.

45. Sun, J. M.; Skorupa, W.; Dekorsy, T.; Helm, M.; Rebohle, L.; Gebel, T. Bright Green Electroluminescence from Tb^{3+} in Silicon Metal-Oxide-Semiconductor Devices. *J. Appl. Phys.* **2005**, *97*, 123513.

46. Charras, G.; Paluch, E. Blebs Lead the Way: How to Migrate without Lamellipodia. *Nat. Rev. Mol. Cell Biol.* **2008**, *9*, 730–736.

47. Downward, J.; Parker, P.; Waterfield, M. D. Autophosphorylation Sites on the Epidermal Growth Factor Receptor. *Nature* **1984**, *311*, 483–485.

48. Jiang, J.; Gu, H. W.; Shao, H. L.; Devlin, E.; Papaefthymiou, G. C.; Ying, J. Y. Bifunctional Fe_3O_4-Ag Heterodimer Nanoparticles for Two-Photon Fluorescence Imaging and Magnetic Manipulation. *Adv. Mater.* **2008**, *20*, 4403–4407.

49. Haes, A. J.; Hall, W. P.; Chang, L.; Klein, W. L.; Van Duyne, R. P. A Localized Surface Plasmon Resonance Biosensor: First Steps toward an Assay for Alzheimer's Disease. *Nano Lett.* **2004**, *4*, 1029–1034.